The Astrophysical Journal, 788:44 (10pp), 2014 June 10 doi:10.1088/0004-637X/788/1/44

MAGNETOACOUSTIC WAVES PROPAGATING ALONG A DENSE SLAB AND HARRIS CURRENT SHEET AND THEIR WAVELET SPECTRA

Hana Mészárosová[1], Marian Karlický[1], Petr Jelínek[1,2], and Ján Rybák[3]
[1] Astronomical Institute of the Academy of Sciences of the Czech Republic, CZ–25165 Ondřejov, Czech Republic; hana@asu.cas.cz
[2] Faculty of Science, University of South Bohemia, CZ–37005 České Budějovice, Czech Republic
[3] Astronomical Institute of the Slovak Academy of Sciences, SK–05960 Tatranská Lomnica, Slovak Republic
Received 2014 March 12; accepted 2014 April 22; published 2014 May 20

ABSTRACT

Currently, there is a common endeavor to detect magnetoacoustic waves in solar flares. This paper contributes to this topic using an approach of numerical simulations. We studied a spatial and temporal evolution of impulsively generated fast and slow magnetoacoustic waves propagating along the dense slab and Harris current sheet using two-dimensional magnetohydrodynamic numerical models. Wave signals computed in numerical models were used for computations of the temporal and spatial wavelet spectra for their possible comparison with those obtained from observations. It is shown that these wavelet spectra allow us to estimate basic parameters of waveguides and perturbations. It was found that the wavelet spectra of waves in the dense slab and current sheet differ in additional wavelet components that appear in association with the main tadpole structure. These additional components are new details in the wavelet spectrum of the signal. While in the dense slab this additional component is always delayed after the tadpole head, in the current sheet this component always precedes the tadpole head. It could help distinguish a type of the waveguide in observed data. We present a technique based on wavelets that separates wave structures according to their spatial scales. This technique shows not only how to separate the magnetoacoustic waves and waveguide structure in observed data, where the waveguide structure is not known, but also how propagating magnetoacoustic waves would appear in observations with limited spatial resolutions. The possibilities detecting these waves in observed data are mentioned.

Key words: magnetohydrodynamics (MHD) – methods: numerical – Sun: corona – Sun: flares

Online-only material: color figures

1. INTRODUCTION

Oscillations and magnetohydrodynamic (MHD) plasma waves play a very important role in many phenomena observed in the solar and stellar atmosphere (e.g., Aschwanden 2004, Stepanov et al. 2012). These waves and oscillations have been analyzed theoretically as well as numerically. The impulsively generated MHD waves and oscillations can be excited by various processes in the solar corona (e.g., by impulsive flare processes). These flare processes can provide either single or multiple sources of perturbations. It has been theoretically predicted (Roberts et al. 1983, 1984) that impulsively generated propagating fast magnetoacoustic waves can be guided by solar coronal structures with enhanced plasma density (e.g., coronal loops) that is acting as the waveguides. These waves form wave trains propagating along their waveguide. The wave train triggered at the initiation site (perturbation point) can be detected at some distance from this site along the waveguide. Time series measured at the detecting point exhibit periodic, quasiperiodic, and decay phases (Roberts et al. 1984). The quasiperiodic phase is generally much stronger in amplitude and shorter in "periodicity" than the earlier periodic phase. This is caused by a dispersion of these waves.

Nakariakov et al. (2004) studied numerically the evolution of the fast magnetoacoustic waves in the dense slab and their wavelet spectra. They found that the wavelet spectra of these waves have the form of "tadpoles" with a narrow tail that precedes a broadband head. The periodic and quasiperiodic phases, pointed out by Roberts et al. (1984), correspond to the tadpole tail and head, respectively, and the start of decay phase corresponds to the tadpole head maximum.

In observations, the wavelet tadpoles were recognized for the first time in the 1999 solar eclipse data (Katsiyannis et al. 2003). Mészárosová et al. (2009a) found the wavelet tadpoles in the gyrosynchrotron radio burst, where all the tadpoles were detected at the same time over the whole frequency range. In subsequent papers Mészárosová et al. (2009b, 2011b) analyzed dm-radio fiber bursts generated by the plasma emission processes. In this case, the wavelet tadpoles slowly drifted with the frequency drift corresponding to the drift of the whole group of fiber bursts. They also found tadpoles with shorter periods and with faster frequency drift that correspond to the drift of individual fiber bursts. More such cases were shown in the paper by Karlický et al. (2013), where a model of the fiber bursts, based on a modulation of the type IV radio burst emission by the fast magnetoacoustic wave trains, was also presented. The wavelet tadpoles were also found in the 15 sources of narrowband dm-radio spikes (Karlický et al. 2011). Using a two-dimensional (2D) MHD model with the Harris current sheet, they concluded that these wavelet tadpoles indicate the fast magnetoacoustic waves propagating in the reconnection plasma outflows. These studies were supported by numerical simulations made by Jelínek & Karlický (2010, 2012), where they compared the evolution of the fast magnetoacoustic waves in a dense slab and Harris current sheet depending on the plasma beta parameter and width of the waveguide. They found that an increase in the distance between the initial perturbation and the detection point increases the length of the tadpole tail. Besides individual solar coronal loops and the current sheet, there are other possible structures that may act as a waveguide. Mészárosová et al. (2013) found wavelet tadpoles indicating the presence of fast magnetoacoustic waves which propagate in the fan structure of

the coronal magnetic null point. Yuan et al. (2013) studied large-scale fast waves in the EUV emission intensity *Solar Dynamics Observatory* (*SDO*)/Atmospheric Imaging Assembly (AIA), where they recognized distinct wave trains with varying periods and wavelengths. Pascoe et al. (2013) used a 2D numerical simulation model of the magnetoacoustic waveguide to consider the effects of an expanding magnetic field. They found that funnel geometry leads to the generation of additional wave trains (formed by the leakage of transverse perturbations) that propagate outside the density structure.

Propagating slow magnetoacoustic waves were observed in coronal loops, e.g., by Hinode/Extreme-ultraviolet Imaging Spectrometer (EIS; Wang et al. 2009a, 2009b) and *Solar and Heliospheric Observatory (SOHO)*/EIT and Transition Region and Coronal Explorer (TRACE; Robbrecht et al. 2001), and in two-ribbon flares (Nakariakov & Zimovets 2011) and were also modeled (e.g., Nakariakov et al. 2000).

In our previous studies, researching the wavelet spectra of the solar radio emission, we recognized, besides "normal" tadpoles corresponding to the fast magnetoacoustic waves, some strange tadpoles with additional features, which occurred several times. These additional features are superimposed on the wavelet spectrum of the normal tadpoles. Although some of these features could be formed by chance or by some kind of signal superpositions or, in some cases, by a high level of artificial noise, their relatively frequent occurrence (observed by independent instruments) leads to a question about their real meaning. Therefore, in the present study we carried out an extended parametric investigation of wave processes in waveguides in order to understand better the link between impulsively generated fast and slow magnetoacoustic waves and the parameters and properties of waveguides and forms of their wavelet spectra. We believe that this study will help in the recognition of magnetoacoustic waves in the solar flare atmosphere and in the determination of waveguide (loop or current sheet) parameters.

This paper is organized as follows. In Section 2, the 2DMHD models and wavelet methods that we used are described. Section 3 presents typical examples of the magnetoacoustic waves in the dense slab and Harris current sheet. Then, in Section 4 we show examples of computed time-varying signals, selected from the parametric investigation of these processes, and their wavelet spectra. Section 5 presents a technique that separates wave structures according to their spatial scales and its application. Finally, the results are summarized in Section 6.

2. TWO-DIMENSIONAL MHD NUMERICAL MODEL AND WAVELET METHODS

2.1. Governing Equations and Numerical Solutions

We used the 2D MHD numerical model presented in Jelínek & Karlický (2010, 2012) and Jelínek et al. (2012) where the plasma dynamics is described by a full set of ideal time-dependent MHD equations (see, e.g., Priest 1982, Chung 2002):

$$\frac{\mathrm{D}\varrho}{\mathrm{D}t} = -\varrho\nabla\boldsymbol{v}, \tag{1}$$

$$\varrho\frac{\mathrm{D}\boldsymbol{v}}{\mathrm{D}t} = -\nabla p + \boldsymbol{j}\times\boldsymbol{B}, \tag{2}$$

$$\frac{\mathrm{D}\boldsymbol{B}}{\mathrm{D}t} = (\boldsymbol{B}\times\nabla)\boldsymbol{v}, \tag{3}$$

$$\frac{\mathrm{D}U}{\mathrm{D}t} = -U(\gamma-1)\nabla\times\boldsymbol{v}, \tag{4}$$

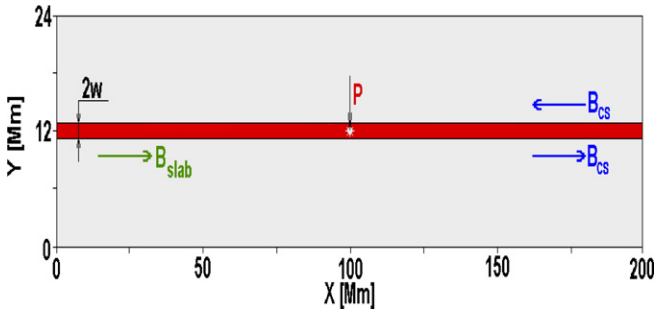

Figure 1. Scheme of a 2D numerical box with a waveguide (in dark) in its center. The length X of the numerical box and waveguide is 200 Mm. The width Y of the numerical box is 24 Mm, and w indicates the half-width of the waveguide. The initial perturbation P is located in the center of the waveguide ($X = 100$ Mm). Arrows show the magnetic field orientation in the dense slab $B_{\rm slab}$ and in the Harris current sheet $B_{\rm cs}$.

(A color version of this figure is available in the online journal.)

$$\nabla\times\boldsymbol{B} = 0, \tag{5}$$

where $\mathrm{D}/\mathrm{D}t \equiv \partial/\partial t + \boldsymbol{v}\times\nabla$ is the convective time derivative, ϱ is a mass density, $\boldsymbol{v}$ is flow velocity, $\boldsymbol{B}$ is the magnetic field, and the adiabatic coefficient $\gamma = 5/3$. The current density, $\boldsymbol{j}$, in Equation (2) is expressed as

$$\boldsymbol{j} = \frac{1}{\mu_0}(\nabla\times\boldsymbol{B}), \tag{6}$$

where μ_0 is the magnetic permeability of free space. The specific internal energy, U, in Equation (4) is given by

$$U = \frac{p}{(\gamma-1)\varrho}, \tag{7}$$

where p is the pressure.

The magnetohydrodynamic equations (1)–(4) were transformed into a flux-conserving form (Chung 2002) and solved numerically. We used two types of numerical codes. The first one is based on a modified two-step Lax–Wendroff algorithm (Kliem et al. 2000). In this code the simulation box (see Figure 1) was covered by a uniform grid with 2500× 300 cells. The cell size in both the X and Y directions was equal to 0.08 Mm, and the numerical time step was $\Delta t = 0.044$ s. This code was used for all computations in this parametric study. To verify these computations in selected cases, we used the FLASH code (Fryxell et al. 2000; Lee & Deane 2009; Lee 2013), which implements second- and third-order unsplit Godunov solvers and adaptive mesh refinement (AMR; see, e.g., Chung 2002; Murawski 2002). As we used AMR, the minimal grid sizes are found to be $\min(\Delta x) = \min(\Delta y) = 0.03$ Mm. In both codes the open boundary conditions were applied. The waveguide half-widths in both waveguides (dense slab and current sheet) were chosen as $w = 0.5$, 1.0, and 2.0 Mm.

2.1.1. Initial Conditions and Equilibrium

Initial conditions were selected according to solar flare conditions and perturbations that generate sausage magnetoacoustic waves. Moreover, to see the differences between magnetoacoustic waves in the dense slab and Harris current sheet, we tried to make both waveguides as similar as possible.

2.1.2. Dense Slab

The dense slab is embedded in a magnetic environment with a magnetic field given by the plasma beta parameter

$$\beta = \frac{p}{p_{\rm mag}} = \frac{2\mu_0 p}{B^2}, \quad (8)$$

where β is assumed to be 0.1. The magnetic field $B_{\rm slab}$ is parallel to the X axis (arrow in Figure 1) and is assumed to be constant in the entire simulation region ($B_{\rm slab} = 3.5 \times 10^{-3}$ T). The dense slab is considered in equilibrium; therefore, for constant magnetic field the kinetic pressure is also constant everywhere. This also means that the temperature profile across the slab is inverse to the profile of the density.

The mass density profile is considered to be constant along the X axis and is expressed along the Y axis by the formula (Nakariakov & Roberts 1995)

$$\varrho(X, Y) = \varrho_0 + (\varrho_{\rm slab} - \varrho_0) \times {\rm sech}^2 \left\{ \left[\frac{(Y - Y_P)}{w} \right]^{\alpha} \right\}, \quad (9)$$

where the power index $\alpha = 8$ determines the steepness of the profile, $Y_P = 12$ Mm is the dense slab center in the Y direction, and w is the half-width of the dense slab.

We selected the parameters in and out of the dense slab as follows: the mass density $\varrho_{\rm in} = 6.69 \times 10^{-11}$ kg m^{-3} (electron density $n_e = 10^{16}$ m^{-3}) and $\varrho_{\rm out} = 6.08 \times 10^{-12}$ kg m^{-3}, temperature $T_{\rm in} = 0.45$ MK and $T_{\rm out} = 5$ MK, the Alfvén velocity $v_{\rm A-in} = 0.39$ Mm s^{-1} and $v_{\rm A-out} = 1.28$ Mm s^{-1}, and the sound velocity $c_{\rm s-in} = 0.11$ Mm s^{-1} and $c_{\rm s-out} = 0.37$ Mm s^{-1}.

2.1.3. Harris Current Sheet

The magnetic field in the Harris current sheet is given by

$$\mathbf{B} = B_{\rm out} \tanh \left[\frac{(Y - Y_P)}{w} \right] \hat{\mathbf{e}}_X, \quad (10)$$

where $B_{\rm out}$ is the magnetic field at $Y \to \infty$ and w is the half-width of the current sheet (see also Figure 1). Magnetic field $B_{\rm out}$ is determined from (Jelínek & Karlický 2012)

$$B_{\rm out} = \sqrt{\frac{2\mu_0 p_{\rm cs}}{1 + \beta}}. \quad (11)$$

The kinetic pressure at the center of the current sheet $p_{\rm cs}$ is calculated from the plasma density at the center of the current sheet $\varrho_{\rm cs}$. The plasma beta parameter β outside of the current sheet is assumed to be 0.1.

Because of the zero magnetic field at the center of the current sheet $B_{\rm cs} = 0$, one can calculate, from the condition of equilibrium

$$p + \frac{B^2}{2\mu_0} = {\rm const}, \quad (12)$$

that the distribution of the mass density in the simulation box is

$$\varrho(x, y) = \varrho_{\rm cs} - \frac{m B_x^2(y)}{2\mu_0 k_{\rm B} T}, \quad (13)$$

where m is the proton mass and $k_{\rm B}$ is the Boltzmann constant.

In our computations the magnetic field $B_{\rm out}$ is chosen as $B_{\rm out} = 3.5 \times 10^{-3}$ T. The parameters in the center, at the $Y = w$, and out of the current sheet are as follows: mass density $\varrho_{\rm c} = 6.69 \times 10^{-11}$ kg m^{-3}, $\varrho_w = 3.32 \times 10^{-11}$ kg m^{-3}, and $\varrho_{\rm out} = 6.08 \times 10^{-12}$ kg m^{-3}; the temperature and sound speed are constant in the whole numerical box $T = 5$ MK and $c_{\rm s} = 0.37$ Mm s^{-1}; the Alfvén velocity $v_{\rm A-c} = 0$, $v_{\rm A-w} = 0.40$ Mm s^{-1}, and $v_{\rm A-out} = 1.28$ Mm s^{-1}; and the plasma beta parameter $\beta_{\rm c} = \infty$ and $\beta_{\rm w} = 0.96$.

2.1.4. Perturbation

We perturbed the initial equilibrium (with $\boldsymbol{v} = 0$) by the Gaussian pulse in the Y component of the velocity. The perturbation point P (Figure 1), where the velocity is perturbed, was located at the center ($X_P = 100$ Mm, $Y_P = 12$ Mm) of the numerical box. This initial velocity pulse v_Y followed a profile (e.g., Nakariakov et al. 2004, 2005)

$$v_Y = A_0 \frac{Y}{\lambda_X} \exp \left[-\frac{(X - X_P)^2}{\lambda_X^2} \right] \exp \left[-\frac{(Y - Y_P)^2}{\lambda_Y^2} \right], \quad (14)$$

where $A_0 = 1.5 \times 10^4$ m s^{-1} is the initial amplitude of the pulse and λ_X and λ_Y are the half-widths of the velocity pulse in the X and Y directions, respectively. We used the size of the perturbation half-widths $\lambda_X = 1.5$ Mm and $\lambda_Y = 0.5$ Mm in our whole study (except Section 4.1).

2.2. Wavelet Methods

We used wavelet power spectra for an analysis of time series collected in selected points along the waveguide at different distances from the initial perturbation point P. These power spectra in our entire study are based on the wavelet analysis technique (Torrence & Compo, 1998) with the Morlet mother function with the parameter $\omega = 6$.

In this study we used wavelet power spectra where both the cone of influence (COI; edge effects become important due to finite-length time series) and the confidence level (CL) relative to red noise were taken into account. In each time series, only the regions outside the COI with CL above 99% are considered significant. Thus, we studied only the most dominant characteristic wavelet signatures.

3. TYPICAL EXAMPLES OF PROPAGATING MAGNETOACOUSTIC WAVES IN THE DENSE SLAB AND HARRIS CURRENT SHEET

Figure 2 shows a time evolution of the density perturbations propagating along the dense slab (left part) and Harris current sheet (right part) at four times: 0.5, 50, 100, and 150 s after they were triggered by the initial perturbation in the center of the waveguide (marked by P). The half-width of both waveguides is $w = 1$ Mm. (Note that there are also negative perturbation peaks similar to the positive ones, but they are only partly visible in the figure.) Analyzing the properties of these perturbations (propagation velocities, dispersions, and the phases between the density and magnetic field perturbations) for all computed variables and comparing them to theoretical studies (e.g., Roberts et al. 1984), we recognized here three types of waves: the fast magnetoacoustic waves (marked by F), the slow magnetoacoustic waves (marked by S), and the nonpropagating wave at the location of the initial perturbation (marked by I). Both the fast and slow magnetoacoustic waves propagate from the center of the waveguide (location of the initial perturbation) in opposite directions toward the ends of the waveguide ($X = 0$ and 200 Mm). While the fast magnetoacoustic waves F consist of

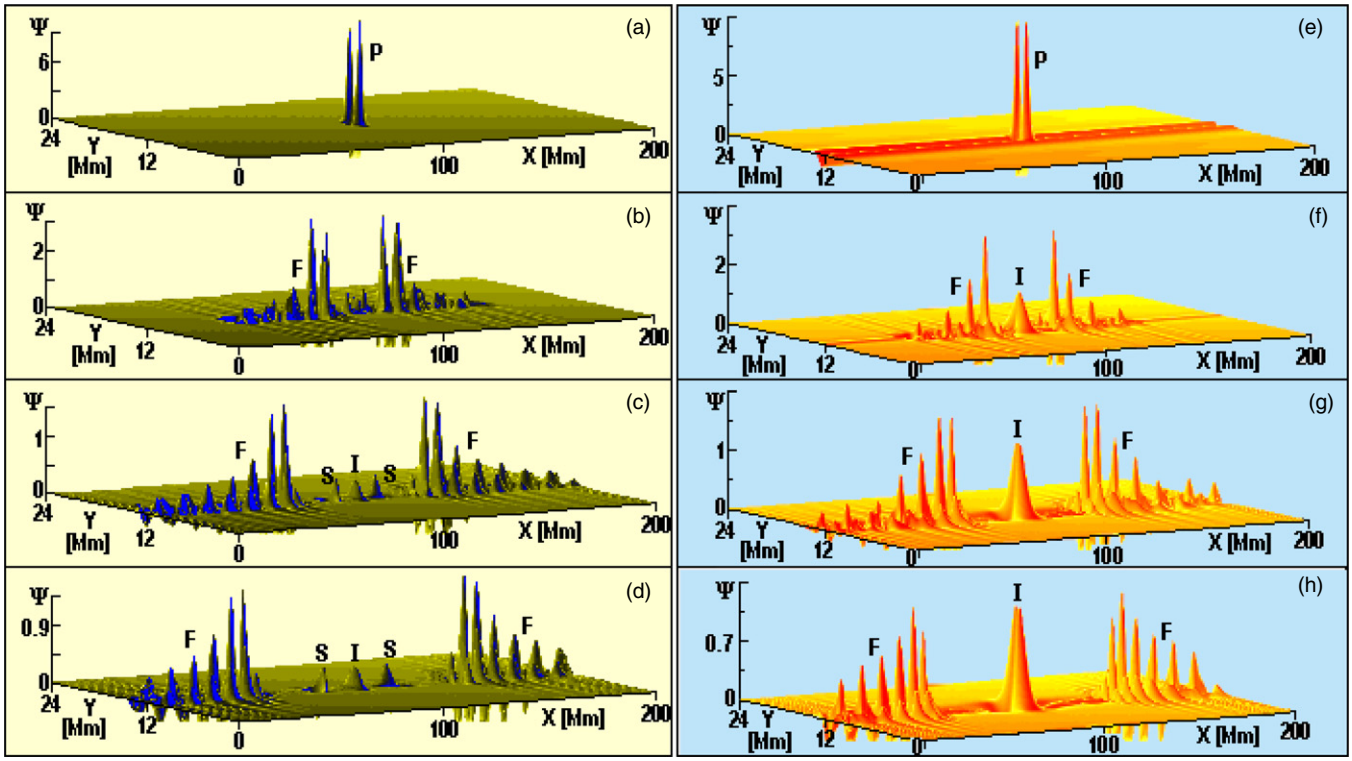

Figure 2. Spatial evolution of the fast F and slow S magnetoacoustic waves propagating in the dense slab (panels (a)–(d)) and the Harris current sheet (panels (e)–(h)) expressed as $\Psi = 10^{-3}(\varrho - \varrho_0)/\varrho_0$, where ϱ is the density and ϱ_0 is the initial density. In both cases, the waveguide half-width w is 1 Mm. The initial perturbation P is generated in the center of waveguide ($X = 100$ Mm, $Y = 12$ Mm). Panels in both columns show propagating waves at times 0.5 s (panels (a) and (e)), 50 s (panels (b) and (f)), 100 s (panels (c) and (g)), and 150 s (panels (d) and (h)) after their generation by the initial perturbation. The peak I remains at the site of the initial perturbation.
(A color version of this figure is available in the online journal.)

many peaks (wave train), where the smallest peaks propagate as the first ones along the waveguide with the highest speed, the slow magnetoacoustic waves S occur only as single peaks during the entire evolution process. Such behavior is a natural effect of the dispersive and nearly nondispersive properties of the fast and slow magnetoacoustic waves, respectively.

The nonpropagating peak I differs for the slab and current sheet. In the dense slab this peak I (e.g., Figure 2(d)) is a single peak with small amplitude (comparable to the amplitudes of slow waves) and is seen only in density perturbation records. On the other hand, in the current sheet the peak I is relatively strong and has a double-peak structure (e.g., Figure 2(h)). It appears in all physical variables, but with different structural complexities. Both these peaks I remain at the site of the initial perturbation P during the entire simulation, and one initial perturbation causes one nonpropagating peak I.

4. TEMPORAL EVOLUTION OF THE FAST MAGNETOACOUSTIC WAVES AND THEIR WAVELET SPECTRA

Time series of all physical variables were collected at detection points with a distance of 5 Mm from each other along the whole waveguide, where a wave train of the fast magnetoacoustic wave propagates. For the purpose of this paper, we selected time series of a ratio of the density perturbation $(\varrho - \varrho_0)$ and the initial density ϱ_0, i.e., $\Psi = 10^{-3}(\varrho - \varrho_0)/\varrho_0$. From these series we computed the wavelet power spectra at all detection points. Typical examples are summarized in Figure 3, where the time series and their wavelet spectra with tadpole patterns for the dense slab (panels (a)–(c)) and Harris current sheet (panels (d)–(f)) are shown. The transverse half-width of the initial perturbation is in all cases $\lambda_Y = 0.5$ Mm. The wavelet spectra were computed for three values of the half-width of the waveguide, $w = 0.5$ Mm (panels (a) and (d)), $w = 1.0$ Mm (panels (b) and (e)), and $w = 2.0$ Mm (panels (c) and (f)), and at three detection points located 10 Mm (panels (a1)–(f1)), 30 Mm (panels (a2)–(f2)), and 50 Mm (panels (a3)–(f3)) from the initial perturbation site. Here, we can see that characteristic time periods of guided waves t_p increase with an increase of the width of the dense slab, in agreement with the relation $t_p = 2.6w/v_{\mathrm{A-in}}$ (Roberts et al. 1984, Jelínek & Karlický 2012). However, here, we found that for the Harris current sheet this period is $t_p \approx 2.6w/v_{\mathrm{A-w}}$, where $v_{\mathrm{A-w}}$ is the Alfvén velocity at the half-width w of the current sheet. The wavelet spectra also confirm that tadpole tails become longer, increasing the distance between the initial perturbation and detection points.

In addition to these known facts, there are new details concerning a form of the main tadpole and also additional structures. For example, in the wavelet spectra corresponding to the narrow waveguide ($w = 0.5$ Mm) the tadpole heads are suppressed for both the dense slab and current sheet. This is consistent with the results of modeling presented in Nakariakov et al. (2005). The situation differs for the wavelet spectra with a broader waveguide ($w = 1.0$ Mm), where the tadpole heads are more distinctly expressed for both the slab and current sheet. The additional structures are small (arrow 1 in Figure 3) for the slab and more significant for the current sheet (arrows 6 and 8). Furthermore, for the broad waveguide ($w = 2.0$ Mm) all tadpole heads are accompanied by additional structures (arrows 2–5, 7, and 9). There is a significant difference between additional structures for the dense slab and current sheet. While in the slab

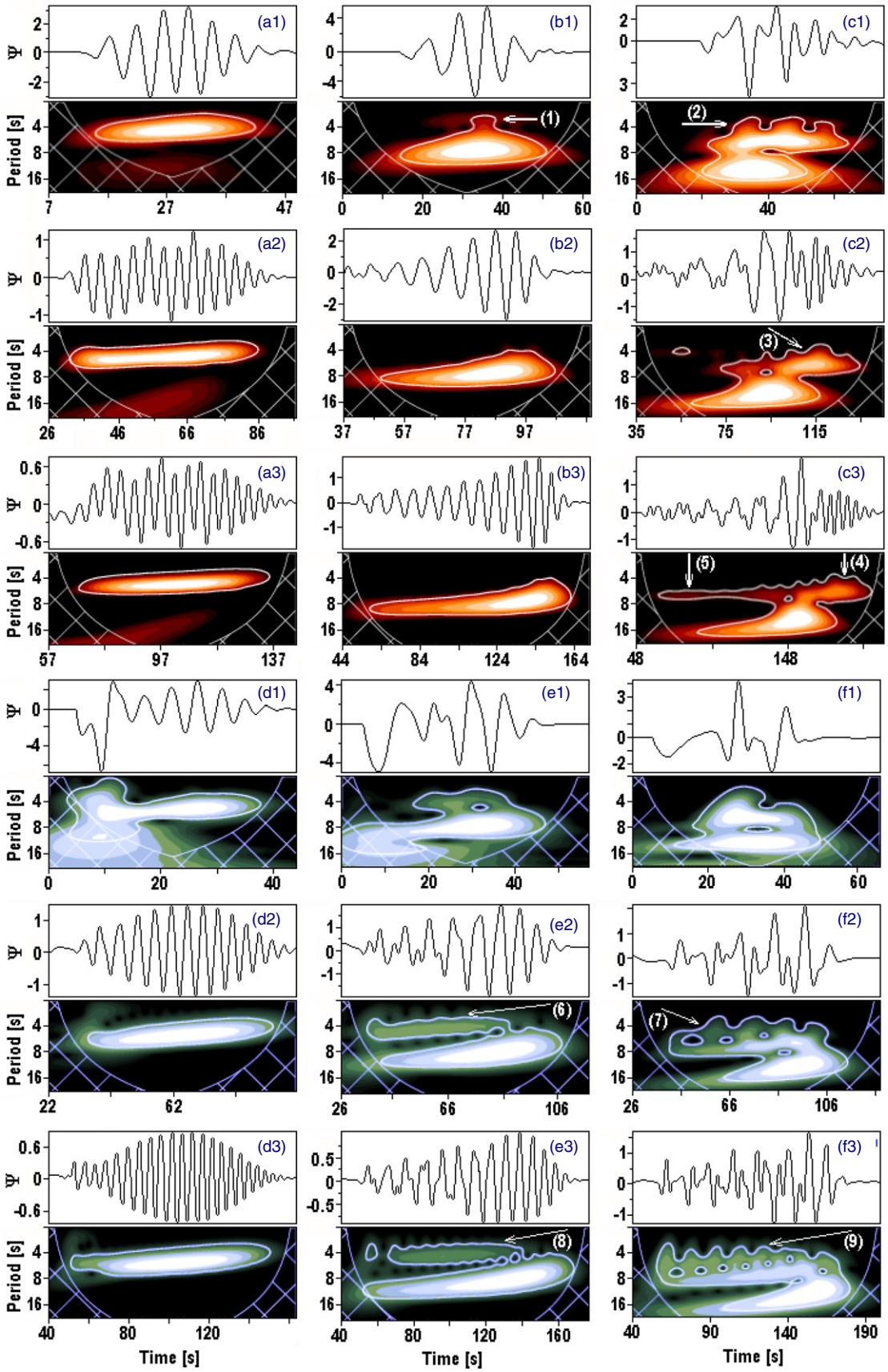

Figure 3. Time series of $\Psi = 10^{-3}(\varrho - \varrho_0)/\varrho_0$ and their wavelet spectra in the dense slab (panels (a)–(c)) and Harris current sheet (panels (d)–(f)) depending on the half-width of the waveguide $w = 0.5$ Mm (panels (a) and (d)), $w = 1.0$ Mm (panels (b) and (e)), and $w = 2.0$ Mm (panels (c) and (f)) and for detection points located 10 Mm (panels (a1)-(c1) and (d1)–(f1)), 30 Mm (panels (a2)–(c2) and (d2)–(f2)), and 50 Mm (panels (a3)–(c3) and (d3)–(f3)) from the initial perturbation. Some wavelet tadpole patterns show various types of additional structures (arrows 1–9).

(A color version of this figure is available in the online journal.)

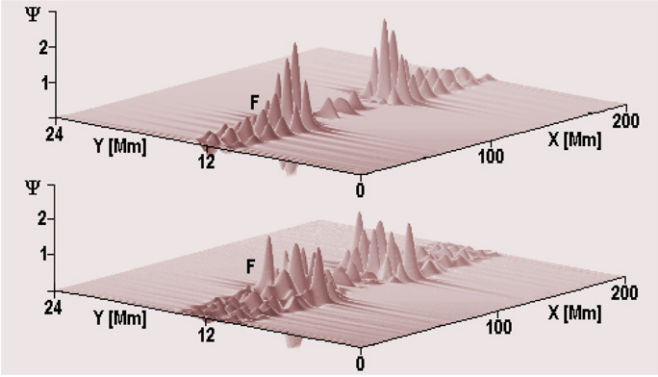

Figure 4. Spatial distribution of $\Psi = 10^{-3}(\varrho - \varrho_0)/\varrho_0$ along the dense slab at a time of 100 s after the initial perturbation, where F means the fast magnetoacoustic wave train. Top and bottom panels are for half-widths $w = 1.0$ Mm and $w = 2.0$ Mm, respectively.

(A color version of this figure is available in the online journal.)

case the additional structures (arrows 2–4) are always delayed after the tadpole head maximum, in the current sheet case the additional structures (arrows 6–9) always precede the tadpole head maximum. Sometimes, we can see the preceding additional structures also in the slab case (arrow 5), but they are always accompanied by the delayed ones. The additional structures (arrows 1–9) have shorter periods than the period of the main tadpole. They are connected to an appearance of additional wave trains in the waveguide, as shown in Figure 4. While the case with the waveguide half-width $w = 1$ Mm (top panel) shows a rather simple wave train, the case with the waveguide half-width $w = 2$ Mm (bottom panel) displays several mixed wave trains. In such a case, the main wave train at the waveguide center ($Y \approx 12$ Mm) causes the main tadpole, and the additional wave trains cause the additional structures in the wavelet spectrum. Note that the same results as presented in Figures 2 and 3 were also obtained using the FLASH code (see Section 2).

The slow magnetoacoustic waves are expressed as a simple "blob" on the wavelet spectrum. Because their amplitude is much smaller than that of the fast magnetoacoustic waves, they appear on the wavelet spectrum only at low confidence levels.

4.1. Effects of Different Half-widths of Perturbations

There is a question of whether a form of the wavelet tadpoles can be affected by different types of initial perturbation, e.g., by a change in the ratio between the transverse half-width of perturbation λ_Y and the half-width of waveguide w. Therefore, we computed time series of $\Psi = 10^{-3}(\varrho - \varrho_0)/\varrho_0$ and their wavelet spectra (see Figure 5) for the dense slab (panels (a) and (b)) and Harris current sheet (panels (c) and (d)), where the perturbation half-width λ_Y was selected as $\lambda_Y = 0.5w$ (panels (a1)–(d1)), $\lambda_Y = w$ (panels (a2)–(d2)), and $\lambda_Y = 2w$ (panels (a3)–(d3)). The wavelet tadpoles were computed for the waveguide half-widths $w = 1.0$ Mm (panels (a1)–(a3) and (c1)–(c3)) and $w = 2.0$ Mm (panels (b1)–(b3) and (d1)–(d3)). All time series are collected at the detection point located 30 Mm from the initial perturbation point.

As seen in Figure 5, when the waveguide half-width is $w = 1.0$ Mm, there are no significant additional structures for

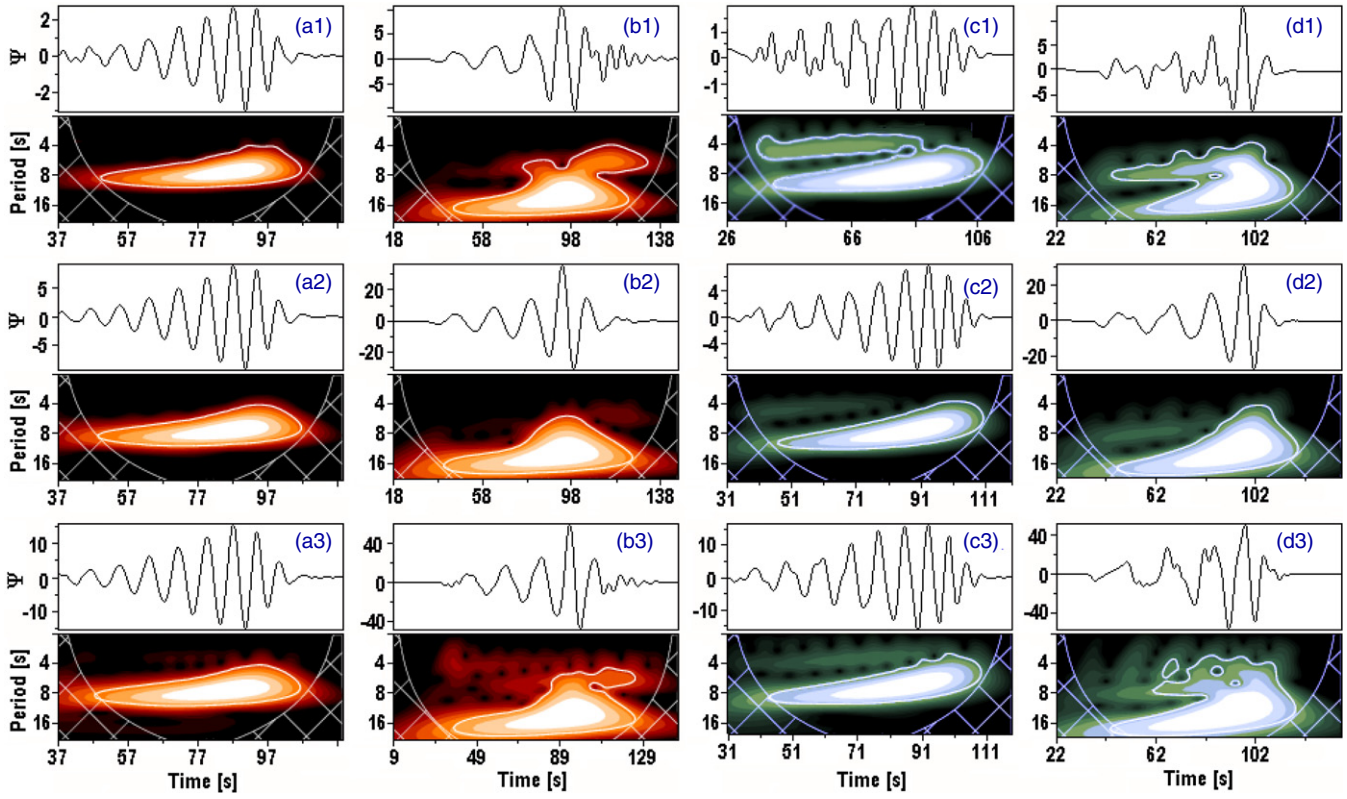

Figure 5. Time series of $\Psi = 10^{-3}(\varrho - \varrho_0)/\varrho_0$ and their wavelet spectra depending on the ratio between the transverse half-width of the perturbation λ_Y and the half-width of the waveguide w: $\lambda_Y = 0.5w$ (panels (a1)–(d1)), $\lambda_Y = w$ (panels (a2)–(d2)), and $\lambda_Y = 2w$ (panels (a3)–(d3)). Wavelet spectra for the dense slab (panels (a) and (b)) and the Harris current sheet (panels (c) and (d)) are computed for $w = 1.0$ Mm (panels (a) and (c)) and $w = 2.0$ Mm (panels (b) and (d)). All time series are collected in the detection point located 30 Mm from the initial perturbation.

(A color version of this figure is available in the online journal.)

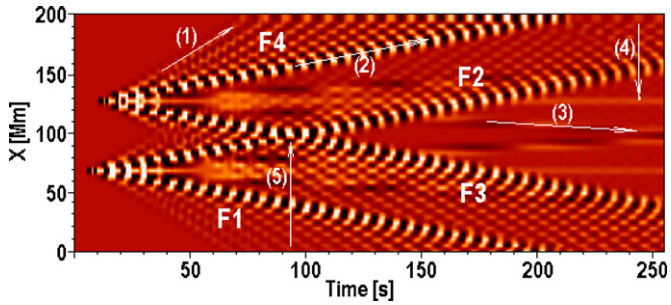

Figure 6. Dynamic spectrum of time series of $\Psi = 10^{-3}(\varrho - \varrho_0)/\varrho_0$ collected at all points along the density slab, i.e., for $X = 0$–200 Mm with a grid distance of 5 Mm. The first and second perturbations are generated 5 and 10 s after the start of computation, and they are located at the points with $X = 70$ and 130 Mm ($Y = 12$ Mm), respectively. Both perturbations generate four fast ($F1$–$F4$) and four slow magnetoacoustic waves. Waves $F2$ and $F3$ propagate toward the waveguide center ($X = 100$ Mm), and they interact at a time of 93 s (arrow 5). The fastest and slowest spectral components of wave $F4$ are shown by arrows 1 and 2, respectively. Arrow3 shows one of the slow magnetoacoustic waves. Arrow4 displays the nonpropagating peak I seen, e.g., in Figure 2.

(A color version of this figure is available in the online journal.)

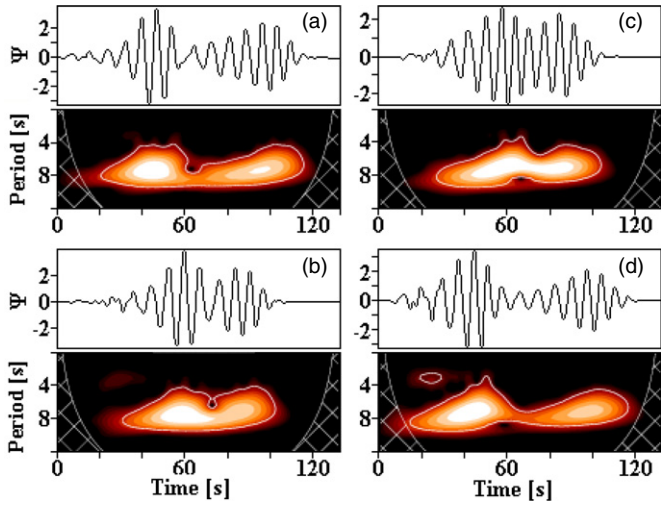

Figure 7. Wavelet spectra corresponding to a mutual interaction between two fast magnetoacoustic waves in the dense slab. Panels (a), (b), (c), and (d) present the wavelet spectra of time series of $\Psi = 10^{-3}(\varrho - \varrho_0)/\varrho_0$ collected at points with $X = 90$, 95, 105, and 110 Mm, respectively.

(A color version of this figure is available in the online journal.)

the dense slab (panels (a1)–(a3)). In case of the current sheet, there are additional structures only if the perturbation half-width is smaller than that of the waveguide (panel (c1)). When the waveguide half-width is $w = 2.0$ Mm (panels (b1)–(b3) and (d1)–(d3)), then the additional structures appear in all cases, except the case where the perturbation and waveguide half-widths are the same. In such a case, the tadpole head is extended toward shorter periods (see panels (b2) and (d2)).

We also made computations for the dense slab and Harris current sheet with the waveguide half-widths $w = 0.5$ Mm for all values of λ_Y as in Figure 5. In these cases none of the tadpoles have any additional structures, and all have suppressed heads regardless of the half-width of the perturbation.

4.2. Mutual Interactions of Propagating Magnetoacoustic Waves

We also studied wavelet spectra for the case with two perturbations in one waveguide, which generate several interacting waves. We considered the same numerical box as in Figure 1, with the dense slab having a half-width of 1.0 Mm.

An example of such wave interactions is shown in Figure 6, where the density perturbation $\Psi = 10^{-3}(\varrho - \varrho_0)/\varrho_0$ is excited. This dynamic spectrum is computed from time series collected at detection points along the waveguide at locations $X = 0$–200 Mm and $Y = 12$ Mm. The spatial step between detection points along the X coordinate is 5 Mm. The first and second perturbations were initiated at locations $X = 70$ and 130 Mm, 5 and 10 s after the simulation starting time, respectively. The initial amplitude of both perturbations is the same, i.e., $A_0 = 1.5 \times 10^4$ m s^{-1}. Both perturbations generate two pairs of fast ($F1$–$F4$) wave trains and two pairs of slow waves. As presented in Figure 6, fast waves $F1$ and $F4$ propagate toward the waveguide ends $X = 0$ and 200 Mm, respectively. On the other hand, fast waves $F2$ and $F3$ propagate to the waveguide center ($X = 100$ Mm), where they interact. First, we can see an interaction of the fastest components of these waves, corresponding to the periodic parts of the wave trains and also to tadpole tails in the wavelet spectra. In the following times, slower and slower wave components start to interact. The velocities of the fastest and slowest components of wave $F4$, which are marked by arrows 1 and 2, are 1.0 and 0.35 Mm s^{-1}, respectively. Note that the most distinct and slowest components of waves $F2$ and $F3$, which correspond to the quasiperiodic parts of the wave trains and also to tadpole heads in the wavelet spectrum, interact at a time of 93 s (arrow 5). Arrow3 shows one of the slow waves propagating at a speed of 0.1 Mm s^{-1}. This slow wave has only one component. Arrow4 displays one of the peaks I (see Figure 2), which remains at the location of the initial perturbation ($X = 130$ Mm) during the whole simulation.

Comparing the velocities found for these waves with the assumed Alfvén velocities in and out of the dense slab (v_{A-in} and v_{A-out}) and the sound velocity in the dense slab (c_{s-in}; see Section 2), we can see that the computed velocities agree with those theoretically predicted by Roberts et al. (1984). Namely, the velocities of the fastest and slowest components of the fast wave train should correspond to $v_{A-out} = 1.28$ Mm s^{-1} and $v_{A-in} = 0.39$ Mm s^{-1}, respectively, and the velocity of the slow magnetoacoustic wave should correspond to the sound velocity $c_{s-in} = 0.11$ Mm s^{-1}. Note that a determination of the fastest component of the fast wave train is not very precise because of its very low signal at the arrival time at the detection point.

For the Harris current sheet with the same half-width w, the dynamical spectrum is very similar to that of the dense slab (Figure 6).

The wavelet spectra of an interaction between fast magnetoacoustic waves $F2$ and $F3$ in the dense slab are displayed in Figure 7. Panels (a), (b), (c), and (d) present time series of $\Psi = (\varrho - \varrho_0)/\varrho_0$ collected *near* their interaction region, i.e., at the detection points $X = 90$, 95, 105, and 110 Mm, and their wavelet spectra. The wavelet patterns look like they are composed of two tadpoles. The first tadpole corresponds to the wave train before the interaction of waves, and the second one corresponds to the wave train after the wave interaction. Because waves $F2$ and $F3$ were not initiated at the same time (they are separated by a small delay of 5 s), the interacting wave trains at the interaction site are similar but not the same (not in the same state of evolution). This difference is also found between the wavelet patterns in Figures 7(a) and (d) (and Figures 7(b) and (c)). The wavelet spectrum of this interaction at $X = 100$ Mm is similar to that in panel (b2) of Figure 3.

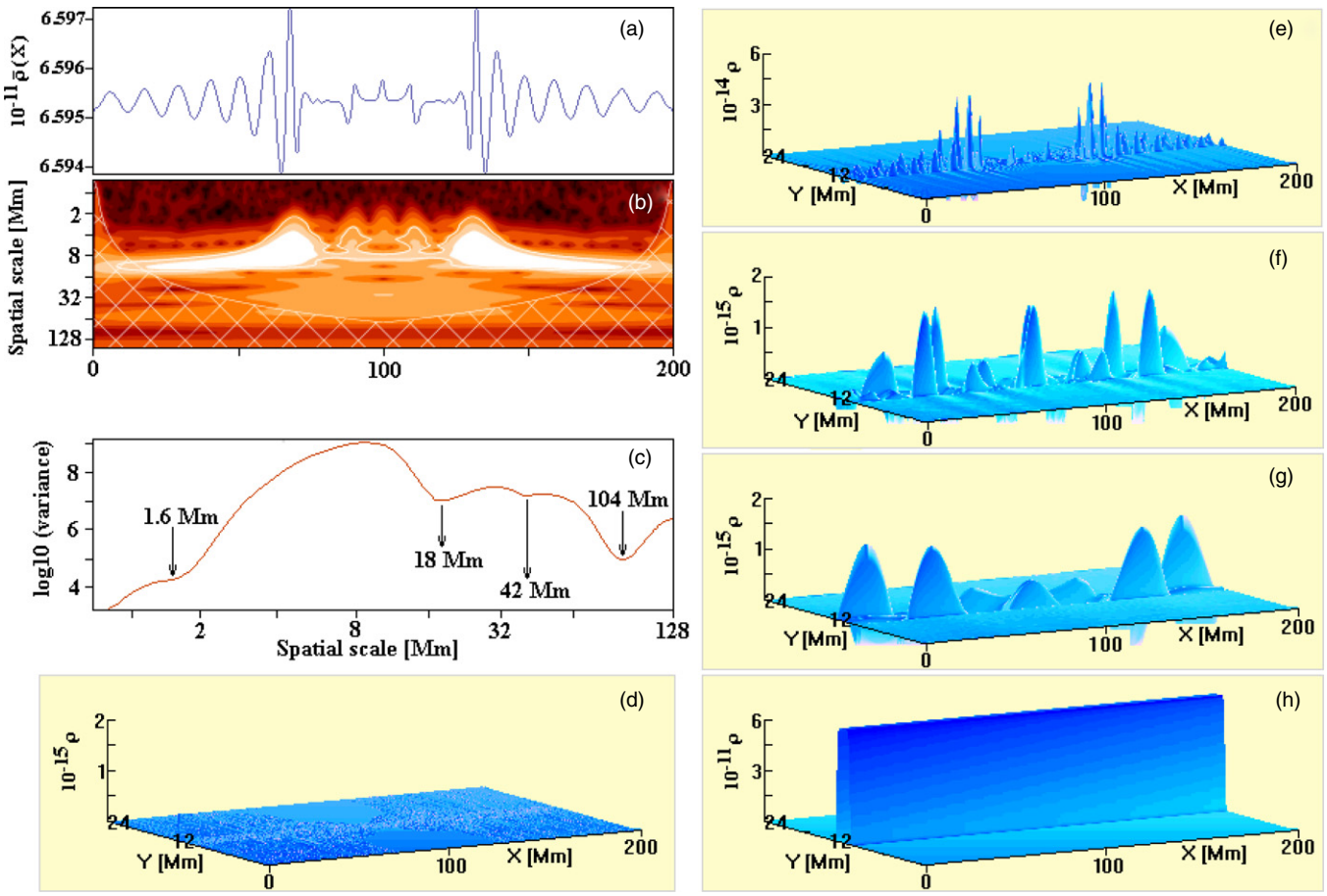

Figure 8. Separation of density variations according to their characteristic spatial scales. Panel (a) shows variations of the averaged density $\bar{\varrho}(X)$ depending on the spatial coordinate X. Panel (b) shows the wavelet power spectrum of the variable $\bar{\varrho}(X)$. Panel (c) presents the global wavelet spectrum with individual minima at 1.6, 18, 42, and 104 Mm. Panel (d) shows the filtered spatial structure for spatial scales <1.6 Mm corresponding to a numerical noise. Panel (e) presents the filtered spatial structure for spatial scales in the range of 1.6–18 Mm, showing both fast and slow magnetoacoustic waves. Panels (f) and (g) present filtered spatial structures with spatial scales in the ranges 18–42 and 42–104 Mm, respectively, showing long spatial components of the waves. Panel (h) presents the filtered spatial structure with spatial scales >104 Mm, showing the original density profile.

(A color version of this figure is available in the online journal.)

(Note that in the ideal case where both waves (with the same A_0) are initiated at the same time, the interacting wave trains at the interaction site will be the same.) Far away from the interaction site (distances >10 Mm) the time series and their wavelet power spectra show two separate tadpoles. In summary, the wavelet spectra of mutual interactions of the fast magnetoacoustic waves depend on the evolution states of the wave trains of both waves at the time of their interaction.

5. MAGNETOACOUSTIC WAVES SEPARATED INTO SEVERAL SPATIAL SPECTRAL COMPONENTS

Generally, perturbations of magnetoacoustic waves are superimposed on an initial waveguide profile. Thus, to display these waves (which have relatively small amplitudes) distinctly, we subtract the initial profile, e.g., the initial density profile ϱ_0. However, we can only make this subtraction in the case of numerical simulations, where the profile ϱ_0 is known. Such a subtraction is impossible to make in observed data, where these initial profiles of the waveguides are not generally known. To mimic a situation with observed data, we analyzed data obtained from our numerical simulations directly, i.e., without any subtractions.

Note that the effect of the line-of-sight (LOS) angle can significantly affect an observed signal. The importance of this effect in the observational manifestation of MHD waves in the optically thin regime was demonstrated in Gruszecki et al. (2012) and Antolin & Van Doorsselaere (2013). The LOS effect is not included in numerical simulations presented in this study.

We used the method based on wavelets as described by Mészárosová et al. (2011a). Generally, this method enables us to separate spatial or time structures according to their spatial or time scales. In the present case, we use this method to separate (filter) the magnetoacoustic waves from computed densities in the dense slab at one selected instant according to characteristic spatial scales.

An example of such a separation is presented in Figure 8, where we analyzed the magnetoacoustic waves at 100 s after the initial perturbation, the same case as shown in Figure 2(c). First, we computed the averaged density $\bar{\varrho}(X)$ (averaged in the dense slab along the Y coordinate, i.e., between $Y_{\min} = 11$ Mm and $Y_{\max} = 13$ Mm), which is dependent on the spatial coordinate X. This averaged density, its spatial wavelet power spectrum, and its global wavelet spectrum are shown in Figures 8(a), (b), and (c), respectively. The wavelet power spectrum displays tadpoles at spatial scales of 1.6–18 Mm. These tadpoles are spatial equivalents of the tadpoles found in time series (Section 4). The global wavelet spectrum shows individual minima at 1.6, 18, 42, and 104 Mm. They enable us to determine the most

characteristic spatial variations of the averaged density $\bar{\varrho}(X)$ (for more details, see Mészárosová et al. 2011a).

We used the determined characteristic spatial scales to divide the spatial variations $\bar{\varrho}(X)$ into five spatial scale intervals: <1.6 Mm, 1.6–18 Mm, 18–42 Mm, 42–104 Mm, and >104 Mm. After an inversion procedure for the wavelet spectra in the entire numerical box in the selected spatial scale ranges, we obtained spatial structures as shown in Figures 8(d)–(h). While the spatial structure shown in the panel (e) (spatial scales 1.6–18 Mm) corresponds to the main spatial components of both the fast and slow magnetoacoustic waves, the structure in panel (h) (spatial scales >104 Mm) corresponds to the initial dense slab. The structure in panel (d) (spatial scales <1.6 Mm) is numerical noise. Besides these structures, in panels (f) and (g) we can see the structures expressing very long spatial components of the magnetoacoustic waves at spatial scales of 18–42 and 42–104 Mm, respectively. These components are interesting because they show how the propagating magnetoacoustic waves would appear in observations with limited spatial resolutions.

6. CONCLUSIONS

Motivated by our previous studies, in which we tried to interpret various forms of the wavelet spectra of observed data, in the present paper we made an extended parametric study of the properties of impulsively generated fast and slow magnetoacoustic waves propagating in the dense slab and Harris current sheet.

The following results were obtained.

1. Both the dense slab and Harris current sheet are good waveguides of magnetoacoustic waves. The dense slab and Harris current sheet with the presented parameters guide the fast magnetoacoustic waves in a similar way. They differ in guiding the slow magnetoacoustic waves. The difference comes from the different magnetic fields and temperature structures of these waveguides.
2. The characteristic period of the fast magnetoacoustic waves is given by $t_p = 2.6w/v_{\mathrm{A-in}}$ in the dense slab and by $t_p \approx 2.6w/v_{\mathrm{A-w}}$ in the Harris current sheet, where $v_{\mathrm{A-in}}$ is the Alfvén velocity inside the dense slab and $v_{\mathrm{A-w}}$ is the Alfvén velocity at the half-width w of the current sheet. Because in our models $v_{\mathrm{A-in}}$ and $v_{\mathrm{A-w}}$ are similar, for the same w in both waveguides, we obtain similar periods and also similar tadpoles in the wavelet spectra. Therefore, from only tadpole forms in an analysis of the observed data, the dense slab and Harris current sheet cases cannot be distinguished.
3. Each fast magnetoacoustic wave forms a wave train where the components with the smallest and largest amplitudes propagate at the highest and lowest speeds, respectively. The slow magnetoacoustic wave propagates as a single peak. It is a natural effect of the dispersive and nearly nondispersive properties of the fast and slow magnetoacoustic waves, respectively.
4. We found a nonpropagating wave at the site of the initial perturbation in both the dense slab and current sheet cases. In the dense slab, this wave had a single structure, with a small amplitude, and was detected only in density perturbation records. In the current sheet this wave was relatively strong and had a double structure. It appeared in all physical variables, but with different structural complexities. This stationary structure is known as the entropy mode (see, e.g., Murawski et al. 2011). We showed that this nonpropagating wave can be detected in spatially resolved data.
5. Comparing the wavelet spectra for the dense slab and current sheet cases, computed for their different half-widths, we found significant differences. For cases with the narrow waveguide ($w = 0.5$ Mm) the tadpole heads were suppressed. For the broader waveguide with $w \approx 1.0$ Mm, the additional structures on wavelet tadpole heads were significant only for the current sheet. For the waveguide with $w \approx 2.0$ Mm, the wavelet tadpole heads were extended by the additional structures. In the dense slab case these additional structures were always delayed after the tadpole head maximum. The current sheet case is the opposite. The additional structures can be explained by additional magnetoacoustic wave trains, which appeared in broader waveguides. Comparing the periods of these features and that of the main tadpole, it looks like these features could be the third harmonics of the main wave train. The tadpoles with additional structures had already been found in observed data. For example, in the paper by Mészárosová et al. (2013), the right panel of Figure 8 shows a wavelet structure similar to the one presented here in panel (b1) of Figure 3.
6. The different half-widths of perturbation can affect the occurrence of the additional structures in broader waveguides $\gtrsim$1.0 Mm. When the perturbation half-width is smaller than that of the waveguide, the additional structures are always significant in the current sheet, while in the dense slab they are only significant for the waveguide half-width $\approx$2 Mm. When the perturbation half-width is greater than that of the waveguide, the additional structures only occur for the waveguide half-width $\approx$2 Mm in both waveguide types. In this case, these structures are suppressed comparing with the previous case. The additional structures vanish if the perturbation half-width is equal or similar to that of the waveguide. Then the tadpole head is extended toward shorter periods, especially for the broad waveguide $\approx$2 Mm. In observed data such wavelet structures have already been observed, e.g., in Figure 3 of Mészárosová et al. (2009b).
7. We studied tadpole patterns corresponding to mutual interactions of waves generated by two perturbations. The dynamical spectrum of these processes revealed (1) two pairs of fast and slow magnetoacoustic waves, (2) many fast wave train components, and (3) the propagating speed of the slow waves as well as the speeds of the components of the fast wave train that belong to the periodic and quasiperiodic wave phases, i.e., to the wavelet tadpole tail and head, respectively. The velocities of the fastest and slowest components of the fast wave train and the slow magnetoacoustic waves agree with those theoretically predicted. The dynamic spectrum of the current sheet is similar to the dynamical spectrum for the dense slab.
8. It was shown that the wavelet spectra of a mutual interaction of the fast magnetoacoustic waves depends on the evolution states of the wave trains of both waves at the time of their interaction.
9. We presented a method based on a wavelet technique that separates the spatial components at one instance that correspond to the magnetoacoustic waves and spatial structure of the waveguide. This method is proposed to search for magnetoacoustic waves in observed spatial imaging data where the waveguide structure is not generally known, where the observing cadence is not sufficient for time series gathering, and when the data space resolution is rather poor.

We hope that all these results help in the correct interpretation of the wavelet spectra of processes connected to magnetoacoustic waves, especially the fast magnetoacoustic waves.

H.M., M.K., and P.J. acknowledge support from grant P209/12/0103 (GA CR), research project RVO:67985815 of the Astronomical Institute AS, and the Marie Curie PIRSES-GA-2011-295272 RadioSun project. The work of J.R. was supported by the Slovak Research and Development Agency under contract APVV-0816-11 and by the Science Grant Agency, project VEGA 2/0108/12. The program of mobility between the academies of the Czech Republic and Slovakia is also acknowledged. The FLASH code used in this work was in part developed by the DOE-supported ASC/Alliances Center for Astrophysical Thermonuclear Flashes at the University of Chicago. The wavelet analysis was performed using software based on tools provided by C. Torrence and G. P. Compo at http://paos.colorado.edu/research/wavelets.

REFERENCES

Antolin, P., & Van Doorsselaere, T. 2013, A&A, 555, A74
Aschwanden, M. 2004, Physics of the Solar Corona: An Introduction (Chichester: Praxis)
Chung, T. J. 2002, Computational Fluid Dynamics (New York: Cambridge Univ. Press)
Fryxell, B., Olson, K., Ricker, P., et al. 2000, ApJS, 131, 273
Gruszecki, M., Nakariakov, V. M., & Van Doorsselaere, T. 2012, A&A, 543, A12
Jelínek, P., & Karlický, M. 2010, IEEE Trans. Plasma Sci., 38, 2243
Jelínek, P., & Karlický, M. 2012, A&A, 537, A46
Jelínek, P., Karlický, M., & Murawski, K. 2012, A&A, 546, A49
Karlický, M., Jelínek, P., & Mészárosová, H. 2011, A&A, 529, A96
Karlický, M., Mészárosová, H., & Jelínek, P. 2013, A&A, 550, A1
Katsiyannis, A. C., Williams, D. R., McAteer, R. T. J., et al. 2003, A&A, 406, 709
Kliem, B., Karlický, M., & Benz, A. O. 2000, A&A, 360, 715
Lee, D. 2013, JCoPh, 243, 269
Lee, D., & Deane, A. E. 2009, JCoPh, 228, 952
Mészárosová, H., Karlický, M., Rybák, J., & Jiřička, K. 2009a, ApJL, 697, L108
Mészárosová, H., Karlický, M., Rybák, J., & Jiřička, K. 2009b, A&A, 502, L13
Mészárosová, H., Rybák, J., & Karlický, M. 2011a, A&A, 525, A88
Mészárosová, H., Karlický, M., & Rybák, J. 2011b, SoPh, 273, 393
Mészárosová, H., Dudík, J., Karlický, M., et al. 2013, SoPh, 283, 473
Murawski, K. 2002, Analytical and Numerical Methods for Wave Propagation in Fluid Media (Singapore: World Scientific)
Murawski, K., Zaqarashvili, T. V., & Nakariakov, V. M. 2011, A&A, 533, A18
Nakariakov, V. M., Arber, T. D., Ault, C. E., et al. 2004, MNRAS, 349, 705
Nakariakov, V. M., Pascoe, D. J., & Arber, T. D. 2005, SSRv, 121, 115
Nakariakov, V. M., & Roberts, B. 1995, SoPh, 159, 399
Nakariakov, V. M., Verwichte, E., Berghmans, D., & Robbrecht, E. 2000, A&A, 362, 1151
Nakariakov, V. M., & Zimovets, I. V. 2011, ApJL, 730, L27
Pascoe, D. J., Nakariakov, V. M., & Kupriyanova, E. G. 2013, A&A, 560, A97
Priest, E. R. 1982, Solar Magnetohydrodynamics (Dordrecht: Riedel)
Robbrecht, E., Verwichte, E., Berghmans, D., et al. 2001, A&A, 370, 591
Roberts, B., Edwin, P. M., & Benz, A. O. 1983, Natur, 305, 688
Roberts, B., Edwin, P. M., & Benz, A. O. 1984, ApJ, 279, 857
Stepanov, A. V., Zaitsev, V. V., & Nakariakov, V. M. 2012, Coronal Seismology1st (Weinheim: Wiley-VCH)
Torrence, C., & Compo, G. P. 1998, BAMS, 79, 61
Wang, T. J., Ofman, L., & Davila, J. M. 2009a, ApJ, 696, 1448
Wang, T. J., Ofman, L., Davila, J. M., & Mariska, J. T. 2009b, A&A, 503, L25
Yuan, D., Shen, Y., Liu, Y., et al. 2013, A&A, 554, A144